ChemComm

COMMUNICATION

View Article Online
View Journal | View Issue

Cite this: *Chem. Commun.*, 2026, 62, 839

Received 1st October 2025,
Accepted 21st November 2025

DOI: 10.1039/d5cc05658f

rsc.li/chemcomm

Advanced halide/sulfide all-solid-state lithium metal batteries with fluorinated interface layer

Shuangwu Xu,[a] Na Chen,[a] You Huang,[a] Dan Sun,[a] Huanhuan Li,[b] Huapeng Sun,[c] Zhiguang Peng,*[a] Yougen Tang,[a] Hehe Zhang*[d] and Haiyan Wang*[a]

The development of solid-state batteries is often hindered by interfacial instability, particularly between the electrolyte and the lithium metal anode. To address this challenge, we fabricate a bilayer solid-state electrolyte composed of Li_3InCl_6 and Li_6PS_5Cl, which demonstrates excellent mutual compatibility and high ionic conductivity. Furthermore, a robust, LiF-rich solid electrolyte interphase (SEI) was pre-formed on the lithium metal anode *via* a pre-treatment strategy in a fluoroethylene carbonate-containing electrolyte. This dual design not only ensures stable interfacial contact but also effectively suppresses interfacial side reactions. When integrated into an all-solid-state lithium metal battery with a $LiCoO_2$ cathode, the assembled cell delivers exceptional cycling stability, retaining over 85% of its initial capacity after 100 cycles at a rate of 0.2C. This work highlights the synergistic role of a compatible bilayer electrolyte and an artificial LiF-rich SEI in enabling high-performance and long-lasting solid-state lithium metal batteries.

In light of the current focus on thermal stability, safety, and energy density in energy storage systems, all-solid-state lithium metal batteries (ASSLMBs) are regarded as a disruptive next-generation technology.[1] By substituting flammable organic liquid electrolytes with non-flammable solid-state electrolytes (SSEs), the risks of leakage and combustion can be effectively mitigated, substantially enhancing overall battery safety.[2,3] Furthermore, the integration of SSEs with the lithium metal anode, which exhibits low density, low electrochemical potential, and high theoretical capacity, enables ASSLMBs to achieve superior energy density and safety performance to those of conventional lithium-ion batteries.[4]

[a] *Hunan Provincial Key Laboratory of Chemical Power Sources, College of Chemistry and Chemical Engineering, Central South University, Changsha 410083, China. E-mail: wanghy419@csu.edu.cn*
[b] *School of Chemistry and Chemical Engineering, Henan Normal University, Xinxiang 453007, P. R. China*
[c] *School of New Energy, Chenzhou Vocational Technical College, Chenjiang Laboratory, Chenzhou, Hunan 423000, China*
[d] *School of Energy and Mechanical Engineering, Nanjing Normal University, Nanjing 210023, China*

SSEs are the core component of ASSLMBs, and their performance and stability have attracted significant research attention.[5] Li_3InCl_6 (LIC) and Li_6PS_5Cl (LPSC) are two representative inorganic SSEs. LIC has high ionic conductivity and excellent electrochemical oxidation stability; however, it suffers from poor reduction stability and low air stability.[6] In contrast, LPSC demonstrates high ionic conductivity but inferior electrochemical oxidation stability.[7] Both electrolytes possess good flexibility, facilitating their processability. To some extent, the properties of LIC and LPSC are complementary, enabling the construction of a high-performance bilayer LIC–LPSC SSE. Zeier and colleagues[8] conducted in-depth studies on the importance of such a bilayer architecture. They emphasized that a halide-based SSE layer between the composite cathode and the sulfide SSE is essential for cycling stability, while a sulfide-based SSE layer adjacent to the anode is also critical for interfacial compatibility. Although LPSC shows better reduction stability than LIC, direct pairing with a lithium metal anode remains challenging in practice. Consequently, researchers often employ Li–In alloys as the anode material due to their electrochemical reversibility and improved interfacial stability with LPSC, which enhances long-term cycling performance.[9] Nevertheless, the introduction of electrochemically inactive elements and the complexity associated with alloy anode fabrication pose obstacles to large-scale industrialization. At the same time, Li–In alloy anodes exhibit limited stability against sulfide-based SSEs under demanding conditions such as high current density, high areal capacity, and extended cycling.[10]

Over decades of development in lithium-ion batteries, the solid electrolyte interphase (SEI) has been critical for stabilizing the anode interface.[11] The incorporation of specific additives, such as fluoroethylene carbonate (FEC), promotes the formation of an SEI layer enriched with LiF, which effectively suppresses further side reactions.[12] However, lithium metal undergoes irreversible reduction reactions with sulfide-based SSEs like LPSC, generating interfacial decomposition products such as Li_2S, Li_3P, and other lithium-containing compounds.[13] The formation of these interphases leads to inhomogeneous lithium deposition and promotes the growth of lithium

dendrites, indicating that such a layer cannot be regarded as a stable or desirable SEI.

In this study, a bilayer SSE was fabricated by cold-pressing LIC and LPSC. Scanning electron microscopy (SEM) images reveal a tight and gap-free interface within the bilayer structure, which facilitates efficient ion transport across the SSE. Moreover, through electrochemical pretreatment of lithium metal in a FEC-containing electrolyte, combined with theoretical calculations and experimental characterization, it is demonstrated that FEC preferentially decomposes to form a SEI rich in LiF. The results confirm that the pretreated lithium metal anode significantly mitigates side reactions between the SSE and the anode. As a result, the optimized anode enables prolonged cycle life in lithium cobalt oxide (LCO)-based ASSLMBs. This work proposes a materials design strategy based on controlled anode pretreatment in liquid electrolytes to generate a high-quality SEI layer, offering a feasible solution to address interfacial instability in ASSLMBs.

As shown in Fig. 1a, the XRD pattern of the as-ball-milled LIC without heat treatment exhibits low crystallinity. This can be attributed to the fact that although high-energy ball milling provides sufficient energy for the reaction between LiCl and $InCl_3$, the material retains a largely disordered structure at this stage. After sintering at 300 °C, the XRD peaks of LIC become more intense and sharper, accompanied by a decrease in full width at half maximum, indicating a transition from a disordered to an ordered crystalline structure. Furthermore, the diffraction pattern closely matches the simulated one for space group *C*2/*m*, confirming the successful synthesis of the target LIC compound.[14] Fig. 1b shows the XRD pattern of LPSC, which can be assigned to $F\bar{4}3m$ space group.[15]

As observed by SEM, the ball-milled LIC powder exhibits a broad particle size distribution, with submicron particles uniformly surrounding larger micron-sized granules (Fig. 1c and Fig. S1). This bimodal distribution facilitates the fabrication of highly dense SSE pellets upon pressing. Following sintering at 550 °C, the material undergoes secondary recrystallization, leading to a general increase in particle size, as evidenced in the LPSC sample (Fig. 1d and Fig. S2). Elemental mapping *via* EDS (Fig. S3 and S4) further confirms the homogeneous distribution of all constituent elements.

Fig. 1e shows a cross-sectional SEM image of the bilayer SSE prepared using a polyetheretherketone (PEEK) mold. Owing to the differences in theoretical density and particle size between the LIC and LPSC materials, the two layers exhibit distinct morphological characteristics after compaction, with a clear interface visible between them. Because of the good flexibility and chemical compatibility of LIC and LPSC, no significant reaction occurs at the interface, which remains continuous and devoid of gaps (Fig. S5). This indicates a high degree of compatibility between LIC and LPSC and suggests strong application potential for the bilayer SSE. The overall thickness of the bilayer SSE is approximately 620 μm, with each layer contributing equally to the total thickness. Elemental mapping *via* EDS (Fig. 1f and Fig. S6) clearly illustrates the stratified structure of the bilayer assembly. The flat and tightly bonded interface facilitates efficient ion transport across the different SSE layers, thereby reducing interfacial resistance.

Ionic transport performance is a critical property of SSEs, as it directly determines the overall performance of ASSLMBs. Fig. 2a presents the electrochemical impedance spectroscopy (EIS) results of pure LIC, LPSC, and LIC–LPSC bilayer SSE measured at 30 °C. The ionic conductivities are determined to be 0.35, 1.45, and 0.45 mS cm^{-1} for LIC, LPSC, and the bilayer SSE, respectively, consistent with previously reported values.[16] Among these, the LPSC SSE shows the highest conductivity, while the bilayer architecture successfully integrates the transport characteristics of both components, resulting in competitive overall ion conduction. The temperature-dependent ionic conductivity of the bilayer SSE was further investigated (Fig. 2b) and is well described by the Arrhenius equation (Fig. 2c). The activation energy for ion conduction is calculated to be 0.42 eV, indicating a low energy barrier favorable for efficient ion transport within the bilayer structure. Therefore, the synergistic mechanism of the bilayer electrolyte in enhancing overall cell performance can be attributed to two key factors: (1) the two electrolytes form a dense, well-defined interface *via* simple cold-pressing, which facilitates rapid and unimpeded Li^+ transport, resulting in high overall ionic conductivity. (2) The LIC and LPSC layers functionally complement each other's electrochemical stability, with the LIC layer stabilizing the cathode interface against oxidation and the LPSC layer improving compatibility with the lithium metal anode, thereby comprehensively suppressing interfacial degradation.

The above results demonstrate the application potential of the bilayer SSE in ASSLMBs; however, the stability of the anode

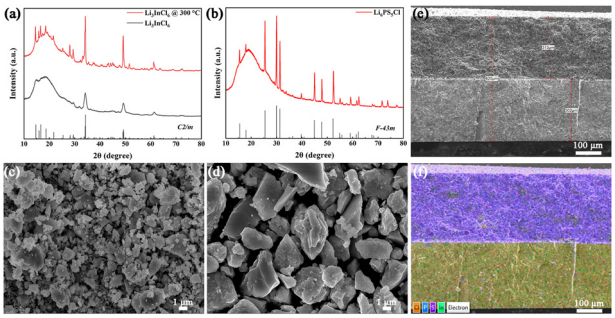

Fig. 1 XRD patterns of (a) LIC and (b) LPSC powders. SEM images of (c) ball-milled LIC and (d) LPSC powders. (e) SEM image and (f) EDS image of the cross-section of the LIC-LPSC bilayer SSE.

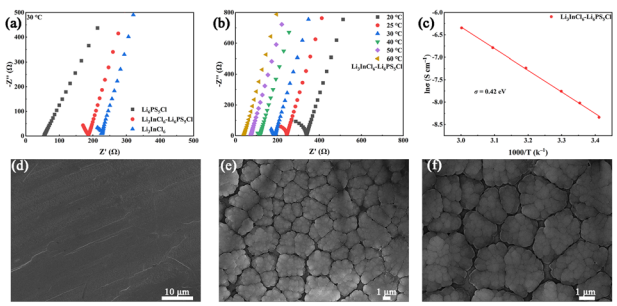

Fig. 2 (a) EIS curves and (b) variable temperature EIS curves of SSEs. (c) Arrhenius plots of ionic conductivities of SSEs. SEM images of the surface of (d) bare Li and (e, f) FEC@Li.

interface remains a critical concern. To address this, a preformed SEI layer was constructed on lithium metal foil by cycling it in a FEC-containing electrolyte. As shown in Fig. 2d and Fig. S7, the pristine Li surface appears smooth and flat. In contrast, the FEC-treated Li (FEC@Li) surface (Fig. 2e and f) exhibits a dense layer of reaction products formed between lithium and the electrolyte. These products are tightly packed, effectively shielding the anode from direct contact with the SSE. EDS analysis (Fig. S8) further confirms a fluorine-rich surface, indicating that FEC promotes the formation of a robust SEI layer.

The energies of the highest occupied molecular orbital (HOMO) and the lowest unoccupied molecular orbital (LUMO) are critical indicators of the electrochemical stability of electrolytes. To clarify the formation mechanism of the SEI in liquid electrolytes, we performed density functional theory (DFT) calculations to determine the HOMO and LUMO energy levels of relevant electrolyte species (Fig. 3a). Among them, FEC exhibits the lowest LUMO energy (−0.161 eV) and a HOMO energy of −8.855 eV, indicating a pronounced tendency toward reduction at the anode. This result suggests that FEC decomposes preferentially on the anode surface, forming LiF—a component with high interfacial energy and a low diffusion barrier for Li^+. Such characteristics enhance Li^+ transport and reduce resistance during plating/stripping. A LiF-rich SEI layer further suppresses ongoing side reactions, thereby improving the cycling stability of the battery.

To elucidate the composition of the SEI on FEC@Li anode, X-ray photoelectron spectroscopy (XPS) analysis was conducted. As shown in Fig. 3b, the elemental composition on the surface of FEC@Li is dominated by Li (32.8 at%), followed by F (26.5 at%), C (26.1 at%), and O (14.6 at%), indicating the involvement of multiple components in the SEI formation. The high-resolution C 1s spectrum (Fig. 3c) exhibits a prominent C–C peak, suggesting the presence of organic species. In the F 1s spectrum (Fig. 3d), the majority of fluorine is assigned to LiF, with minor contributions from $Li_xPF_yO_z$ species.[17] Both compounds originate from the decomposition of $LiPF_6$ at the anode and constitute the inorganic part of the SEI. This is corroborated by the Li 1s spectrum (Fig. 3e), where a strong LiF signal is observed alongside a small amount of Li_2O, attributed to solvent decomposition. In summary, the SEI layer on FEC@Li is rich in inorganic components, particularly LiF, which promotes the formation of a dense and stable passivation layer. This effectively suppresses further side reactions between the SSE and the lithium metal anode, thereby improving the cycling stability of the battery. Furthermore, the chemical composition and structure of the SEI were probed using time-of-flight secondary ion mass spectrometry (ToF-SIMS), a technique well-suited for analyzing thin films with thicknesses in the tens to hundreds of nanometers range. As shown in Fig. 3f–h, the SEI layer on the FEC@Li anode is approximately 20 nm thick. This represents an ideal thickness, which effectively passivates the lithium surface by blocking direct contact with the SSE while still facilitating unimpeded ion transport. The outstanding performance of the pretreated FEC@Li anode can therefore be attributed to this homogeneous, ~20 nm thick SEI layer rich in LiF.

To evaluate the performance enhancement offered by the FEC@Li anode, ASSLMBs were assembled using commercial lithium cobalt oxide (LCO) as the cathode active material. Galvanostatic charge–discharge tests were conducted between 2.6 and 4.2 V. As depicted in Fig. 4a, the initial charge–discharge profiles of the LCO|LIC-LPSC|Li and LCO|LIC-LPSC|FEC@Li cells were measured at 0.1C. The cell with a pristine Li anode exhibits an initial Coulombic efficiency of 84.24% and a discharge capacity of 151.7 mAh g^{-1}. In comparison, the cell with the FEC@Li anode achieves a significantly higher first-cycle Coulombic efficiency of 93.54% and a discharge capacity of 159.1 mAh g^{-1}, indicating effective suppression of initial side reactions. Additionally, the EIS of the two all-solid-state batteries is compared in Fig. S9. The cell with the FEC-modified anode demonstrates a lower interfacial resistance, which is attributed to the stabilized interface resulting from the LiF-rich SEI formed by the FEC pretreatment.

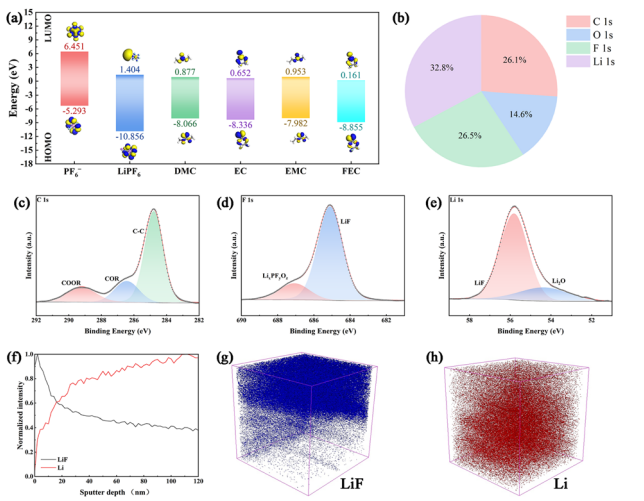

Fig. 3 (a) HOMO–LUMO energy levels of different solvents and additives in the electrolyte. (b) Content ratio of elements distributed on the surface of FEC@Li. XPS spectrum for (c) C 1s, (d) F 1s, and (e) Li 1s of the surface of FEC@Li. (f) Normalized depth profiles of LiF and Li fragments obtained from the FEC@Li anode surface. Three-dimensional reconstruction of the ToF-SIMS sputtered volume showing the distribution of (g) LiF and (h) Li fragments within the SEI.

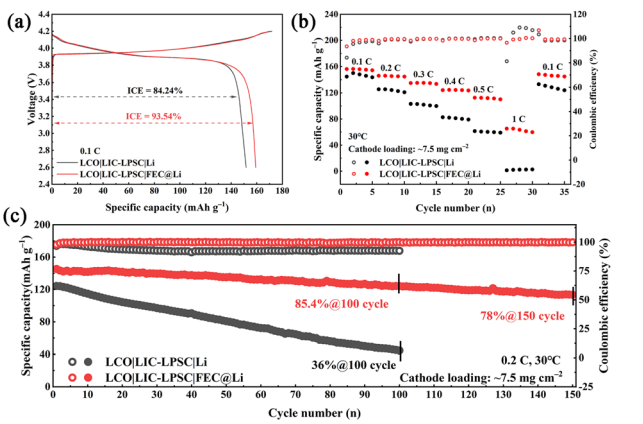

Fig. 4 (a) Initial charge–discharge curves, (b) rate performance, and (c) long cycle performance of LCO|LIC-LPSC|Li and LCO|LIC-LPSC|FEC@Li batteries.

As the current density increases, the FEC@Li-based cell shows moderate capacity decay, delivering discharge capacities of 145.3, 135.4, 124.6, and 112.1 mAh g^{-1} at 0.2C, 0.3C, 0.4C, and 0.5C, respectively, and maintaining 63.5 mAh g^{-1} even at 1C. In contrast, the cell with the untreated Li anode suffers from severe capacity degradation at elevated rates, becoming almost non-functional at 1C. When the current density returns to 0.1C, the FEC@Li cell recovers a discharge capacity of 146.1 mAh g^{-1}, corresponding to 92% of its initial value, whereas the Li anode cell only reaches 128.5 mAh g^{-1} (85% retention).

Long-term cycling performance is shown in Fig. 4c and Fig. S11. After 100 cycles, the FEC@Li cell retains 85.4% of its initial capacity with Coulombic efficiency exceeding 99.8%. Even after 150 cycles, it maintains 78% capacity retention, dramatically outperforming the Li anode cell, which retains only 36% after 100 cycles. As shown in Fig. S12, the cell with the FEC@Li anode demonstrates enhanced electrochemical performance at a current density of 0.5C. In addition, the electrochemical performance of the assembled Li symmetric cells further underscores the critical role of interfacial pretreatment in achieving enhanced cycling stability (Fig. S13). The markedly improved cycling stability underscores the role of a stabilized interface enabled by the FEC pretreatment, highlighting its critical importance in enhancing the performance of ASSLMBs. Fig. S14 shows a cross-sectional SEM image of the cycled Li|LPSC|Li symmetric cell. The image reveals intimate contact between the SSE and the lithium metal anode, with no observable lithium dendrite penetration, confirming excellent interfacial stability. The *in situ* EIS curves in Fig. S15 compare the interfacial stability of the symmetric cells. The Li|LPSC|Li cell shows pronounced instability, evidenced by large and fluctuating impedance, whereas the FEC@Li|LPSC|FEC@Li cell exhibits a stable, low impedance. This directly validates that the LiF-rich SEI formed by FEC pretreatment enhances interfacial kinetics and stability.

In summary, LIC and LPSC, representing two prominent types of inorganic SSEs, demonstrate sufficient flexibility and chemical compatibility to form a coherent bilayer SSE. The intimate, gap-free interfacial contact between these layers facilitates efficient ion transport across the interface. Furthermore, through electrochemical pre-treatment of lithium metal in an FEC-containing electrolyte, a LiF-rich SEI is *in situ* formed on the anode. LiF possesses high interfacial energy and a low Li^+ diffusion barrier, making it an ideal constituent of a robust passivation layer. This SEI prevents direct contact between the SSE and the lithium metal anode, suppresses interfacial side reactions, and significantly enhances cycling stability. The combination of bilayer SSE and pre-treated Li metal anode synergistically ensures both high ionic conductivity and excellent interfacial compatibility. As a result, the LCO-based ASSLMB retains 85.4% of its capacity after 100 cycles at 0.2C. This work offers valuable strategies for stabilizing the anode interface in ASSLMBs.

This research was financially supported by the Hunan Provincial Science and Technology Plan Projects of China (No. 2017TP1001 and No. CX20220158), Chenzhou National Sustainable Development Agenda Innovation Demonstration Zone Provincial Special Project (2023sfq11), the Open Research Fund of School of Chemistry and Chemical Engineering, Henan Normal University. This work was supported in part by the high-performance computing center of Central South University.

H. W. participated in the analysis of results, provided valuable advice to experiment and revised the manuscript. N. C., Y. H., D. S., H. L., H. S., Z. P., Y. T., H. Z. participated in helpful discussions. S. X. participated in the experimental design, synthesized the samples, carried out the characterizations and wrote the manuscript.

Conflicts of interest

There are no conflicts to declare.

Data availability

The data supporting this article have been included as part of the supplementary information (SI). Supplementary information is available. See DOI: https://doi.org/10.1039/d5cc05658f.

Notes and references

1 S. Qiang, J. Chen, S. Huang, H. Xu, X. Zhuo, H. Zhou, A. Yuan, H. Zhou and Y. Qiao, *J. Colloid Interface Sci.*, 2026, **701**, 138722.
2 S. Xu, C. Xie, R. Wang, H. Sun, D. Sun, X. Meng, H. Zhang, L. Che, Y. Tang and H. Wang, *Adv. Funct. Mater.*, 2025, e14032, DOI: 10.1002/adfm.202514032.
3 S. Xu, L. Zhao, Z. Liu, H. Sun, D. Sun, Z. Peng, Y. Tang, W. Wang and H. Wang, *ChemComm*, 2025, **61**, 7887–7890.
4 Y. Shen, S. He, Y. Zhuang, S. Huang, C. Meng, A. Yuan, W. Miao and H. Zhou, *ACS Appl. Nano Mater.*, 2023, **6**, 16873–16881.
5 J. Janek and W. G. Zeier, *Nat. Energy*, 2023, **8**, 230–240.
6 X. Li, J. Liang, J. Luo, M. Norouzi Banis, C. Wang, W. Li, S. Deng, C. Yu, F. Zhao, Y. Hu, T.-K. Sham, L. Zhang, S. Zhao, S. Lu, H. Huang, R. Li, K. R. Adair and X. Sun, *Energy Environ. Sci.*, 2019, **12**, 2665–2671.
7 H. Wan, Z. Wang, W. Zhang, X. He and C. Wang, *Nature*, 2023, **623**, 739–744.
8 C. Rosenbach, F. Walther, J. Ruhl, M. Hartmann, T. A. Hendriks, S. Ohno, J. Janek and W. G. Zeier, *Adv. Energy Mater.*, 2023, **13**, 2203673.
9 P. Lu, Y. Xia, G. Sun, D. Wu, S. Wu, W. Yan, X. Zhu, J. Lu, Q. Niu, S. Shi, Z. Sha, L. Chen, H. Li and F. Wu, *Nat. Commun.*, 2023, **14**, 4077.
10 S. Luo, Z. Wang, X. Li, X. Liu, H. Wang, W. Ma, L. Zhang, L. Zhu and X. Zhang, *Nat. Commun.*, 2021, **12**, 6968.
11 H. Chen, C. Meng, Z. Jiao, A. Yuan and H. Zhou, *Energy Fuels*, 2025, **39**, 4069–4078.
12 R. Damircheli, B. Hoang, V. Castagna Ferrari and C.-F. Lin, *ACS Appl. Mater. Interfaces*, 2023, **15**, 54915–54922.
13 C. Liu, T. Zhang, R. Wang, B. Chen, D. Wang, T. Wang, Z. Yang, T. Liu, Q. Mao, T. Li, J. Zhang, X. Ma and X. Liu, *Adv. Funct. Mater.*, 2025, **35**, 2412144.
14 Z. Song, T. Wang, H. Yang, W. H. Kan, Y. Chen, Q. Yu, L. Wang, Y. Zhang, Y. Dai, H. Chen, W. Yin, T. Honda, M. Avdeev, H. Xu, J. Ma, Y. Huang and W. Luo, *Nat. Commun.*, 2024, **15**, 1481.
15 D. Wang, C. Liu, R. Wang, T. Zhang, B. Chen, T. Wang, Q. Lu, W. Yin and X. Liu, *Angew. Chem., Int. Ed.*, 2025, **64**, e202501411.
16 S. H. Yang, S. Y. Kim and G. Y. Chen, *ACS Energy Lett.*, 2024, **9**, 2212–2221.
17 J. Liu, W. Hao, M. Fang, X. Chen, Y. Dong, Y. Chen, Z. Wang, X. Yue and Z. Liang, *Nat. Commun.*, 2024, **15**, 9356.

